The Hydraulic Conductivity of a Shaped Fracture With Permeable Walls

Daihui Lu[1], Federico Municchi[2], and Ivan C. Christov[1]

[1]School of Mechanical Engineering, Purdue University, West Lafayette, Indiana 47907, USA
[2]School of Mathematical Sciences, University of Nottingham, University Park, Nottingham, NG7 2RD, UK

Key Points:

- Flow-wise variation of fracture aperture is inherently coupled to permeation into surrounding rock
- Hydraulic conductivity and permeation velocity self-consistently calculated via perturbation theory
- Novel analytical expressions for velocity profile and conductivity validated against flow simulations

Corresponding author: Ivan C. Christov, christov@purdue.edu

Abstract

We investigate the flow-wise variation of the hydraulic conductivity inside a non-uniformly shaped fracture within a porous medium. Using lubrication theory for viscous flows, in conjunction with the Beavers–Joseph–Saffman boundary condition at the permeable walls, we obtain an analytical expression for the velocity profile, conductivity, and wall permeation velocity. These predictions highlight the effects of geometric variation (through the local slope of the aperture's flow-wise variation), the permeability of the walls (through a dimensionless slip coefficient), and the effect of flow inertia (through a Reynolds number). The theory is validated against an OpenFOAM® solver for the Navier–Stokes equations subject to a tensorial slip boundary condition, showing good agreement. The mathematical results have implications on system-level (multiscale) modeling of hydraulically fractured reservoirs, in which the Darcy conductivity of each non-uniform passage must be accurately accounted for, throughout the fractured porous rock.

Plain Language Summary

Whether natural or induced, underground fractures have non-uniform shapes. Their cross-sectional area generally decreases slowly in the direction of the flow through the fracture. The walls of the fracture are the surrounding geological porous rock formations. Thus, fluid can leak from the fracture into the surrounding rock matrix. This leakage has significant implications for oil and gas recovery, as well as for evaluating the safety of groundwater reserves residing near fractures. What has not been appreciated in previous studies of flow in fractures is just how the fluid flows into the permeable walls is determined by the rocks' properties, the varying fracture geometry, and the pressure forces driving the flow. This study contributes and validates a mathematical expression for the resistance to flow in a single fracture, elucidating analytically the coupled roles of shape variation and permeation of fluid into the walls. Having such a precise prediction in hand can improve systems-level modeling of complex transport phenomena through fractured rock, which guides the evaluation of the lifespan of an oil or gas reservoir and the efficacy of underground carbon dioxide sequestration, amongst other applications.

1 Introduction

Crude oil and natural gas exist as fluids in large underground reservoirs in sedimentary basins around the world. They occupy the connected porous media within strata of sedimentary rocks, typically sandstones or carbonates (van Golf-Racht, 1982). Over the last decade, hydraulic fracturing ("fracking") of shales has paved the way towards increasing the recoverable reserves of oil and gas in the United States (McBride & Aly Sergie, 2015). During fracking, complex fluids (primarily water-based suspensions with dispersed particulates termed "proppants") (Yew & Weng, 2015; Barbati et al., 2016) are pumped into tight formations (Detournay, 2016; Osiptsov, 2017). Fracking is inherently a multiscale problem (Hyman et al., 2016): as the injected high-pressure fluid enters a rock formation from the well bore, a complex array of cracks of various shapes, sizes, and with flow-wise variations, are created (Yew & Weng, 2015; Rassenfoss, 2015). This network of fractures increases the conductivity of the rock formation by increasing the available flow area (Phillips, 1991; Vincent, 2002). Similarly, in enhanced geothermal systems (Mohais et al., 2012), heat is extracted from hot rocks by flooding the dry fracture network (Mohais et al., 2016; Olasolo et al., 2016). Thus, it is of practical importance, as well as of fundamental scientific interest, to create mathematical models of the conductivity in complex and non-uniform fractures. In this letter, we derive a novel mathematical expression for the conductivity of a shaped fracture with flow-wise geometric variations.

To provide a sense of the scale on which the half-depth h of a fracture may vary with the flow-wise direction x, consider the standard Perkins–Kern–Nordgren (PKN) and the Khristianovitch–Zheltov–Geertsma–de Klerk (KGD) models, which idealize fractures as

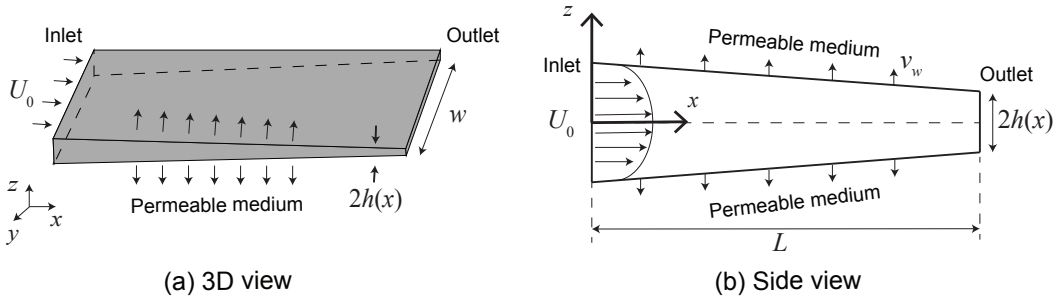

Figure 1. Schematic of a typical fracture flow geometry idealized as a Hele-Shaw cell. The fracture's shape varies appreciably over a "typical" length L, and it has a constant gradient $dh/dx \sim \alpha$, so that the half-depth is $h(x) = h_0 + \alpha x$ (to a linear approximation). The fracture is long and thin meaning $\epsilon = h_0/L \ll 1$ and $\alpha = dh/dx = [h(L) - h_0]/L = \Delta h/L \ll 1$, where $h_0 = h(0)$. Gravity is neglected but, in these schematics, it would act in the transversely in the negative y-direction. The flow is symmetric about the centerline $z = 0$, and primarily in the x-direction, along the fracture. The top and bottom walls $z = \pm h(x)$ are permeable (permeability k_w) and allow a non-zero vertical velocity component v_w at the wall, which is to be determined.

Table 1. Typical dimensions of a hydraulic fracture and typical values of the dimensionless parameters of the hydraulic conductivity model derived in this study.

Quantity	Notation	Value	Remarks
Fracture total length	L_{total}	$100 \sim 1000$ m	(Barbati et al., 2016)
Fracture width	w	$10 \sim 100$ m	(Barbati et al., 2016)
Fracture gap/depth	h_0	$2 \sim 10$ mm	(Barbati et al., 2016)
Typical velocity	U_0	$\lesssim 10^{-3}$ m s^{-1}	(Yew & Weng, 2015, Ch. 1)
Permeability of the wall	k_w	$\lesssim 5 \times 10^{-13}$ m^2	(Barbati et al., 2016)
Hele-Shaw shape variation	$\delta = \alpha/\epsilon$	$\lesssim 10^{-1}$	Slow variation assumption
Hele-Shaw aspect ratio	$\epsilon = h_0/L$	$10^{-4} \sim 10^{-2}$	Using $L = L_{\text{total}}/100$
Hele-Shaw slope	$\alpha = dh/dx$	$\lesssim 10^{-3}$	Using $\lvert\alpha\rvert \sim \epsilon\delta$
Wall slip coeff.	$\phi = \sqrt{k_w}/(ah_0)$	$\lesssim 10^{-3}$	$a = 0.1$
Reduced Reynolds number	$\tilde{Re} = \rho U_0 h_0^2/(\mu L)$	$\lesssim 0.1$	ρ, μ for water

long and narrow elliptical cracks (Rahman & Rahman, 2010). Garagash and Detournay (1999) showed that the fracture tip has a shape with $h(x) \sim (x_{\text{tip}} - x)^{1/2}$ as $x \to x_{\text{tip}} > L$. (The typical fracture geometry we consider has total length L_{total}, appreciable variations in the shape occur over some typical scale $L \ll L_{\text{total}}$, with the tip falling outside the domain in Fig. 1.) Thus, the shape gradient away from the crack tip goes as $\alpha = dh/dx \sim -(x_{\text{tip}} - x)^{-1/2}$. Clearly, as $x \to -\infty$ (away from the crack tip), $|\alpha| \to 0^-$, justifying the small slope assumption $|\alpha| \ll 1$. Typical fracture geometry parameter values are summarized in Table 1, further justifying that, away from the crack tip, $dh/dx \sim |\alpha| \ll \epsilon = h_0/L$; that is, the fracture's typical slope is much smaller than its aspect ratio. (Although our analysis does not depend on the sign of α, we henceforth take $\alpha < 0$ for definiteness.)

The simplest model of fracture conductivity (the parallel-plate model (Zimmerman & Bodvarsson, 1996)) assumes that fracture walls are smooth, impermeable walls with a *constant* gap depth of $2h_0$ (distance between the walls) and span w (length in the transverse direction); see Fig. 1. By analogy to lubricating viscous flow between two plates (the so-called Hele-Shaw model (Bear, 1972)), one can calculate the hydraulic conductivity to be

$\mathcal{K} = h_0^2/3$. Then, the transmissivity of the fracture ($\propto h_0 w \mathcal{K}$) follows the well-known "cubic law" (Witherspoon et al., 1980). However, the flow passages in both naturally (van Golf-Racht, 1982) and hydraulically fractured (Yew & Weng, 2015) formations have a *variable* gap depth $2h(x)$. Generally, the walls of fractures are not parallel (Brown, 1987), in part due to the flow-wise deformation of the fracture due to large injection pressures (Iliev et al., 2008), requiring corrections to Darcy's laws arise via a modified conductivity and transmissivity models (Jin et al., 2017; Wang et al., 2019; Rosti et al., 2020). However, these models are for *impermeable walls*.

The bounding surfaces of a fracture are the porous rock formations themselves, therefore they should not be idealized as impermeable plates (Berkowitz, 1989). Permeation of gas into the matrix, and its subsequent diffusion, affects the late-years productivity of fractured wells (Patzek et al., 2013; Karra et al., 2015). Berman (1953) and Sellars (1955) investigated the effects of a permeable wall in a constant-height channel using the idealized boundary condition of equal prescribed wall-normal velocities. Since then, a large literature has addressed many variations on this problem, including asymmetric wall normal velocities (Terrill & Shrestha, 1964), flow development effects (Brady, 1984), unsteadiness (King & Cox, 2001), and so on. These works rely on reducing the problem to a nonlinear ordinary differential equation, owing to the existence of a similarity transformation in two dimensions (2D). Unfortunately, this technique does *not* work in the case of a depth gradient, such as the present geometry with $h = h(x)$; instead a perturbation solution must be sought (Grotberg, 1984; Wang et al., 2019). Kumar et al. (2016) showed that a similar situation arises if the geometry is uniform but the slip length varies in the flow-wise direction, i.e., $\ell_{\text{slip}} = \ell_{\text{slip}}(x)$. Importantly, imposing the wall-normal velocity *a priori* is a significant limitation of the previous studies because, as Conlisk notes, "[t]he suction velocity at the wall ... must be calculated from the properties of the porous medium" (Conlisk, 2012, p. 162). Here, we take the perturbative mathematical approach, based on the notion of *slow variation* in fluid mechanics (Van Dyke, 1987), to calculate the conductivity of a shaped fracture with permeable walls.

Beavers and Joseph (1967) experimentally characterized pressure-driven (Poiseuille) flow over a naturally permeable surface (i.e., channel flow with porous walls) and proposed a boundary condition to account for the wall permeation. Specifically, they showed that the shear stress balance at the fluid–solid interface can be represented by a first-order (partial) slip boundary condition with slip length $\ell_{\text{slip}} = \sqrt{k_w}/a$, where k_w is the permeability of the porous wall, and a is a dimensionless constant determined by the structure of the material, ranging from 0.1 to 4.0 (Beavers & Joseph, 1967). Taylor (1971) observed that a is not a universal value, but rather it depends on the flow geometry. Saffman (1971) substantiated this observation and generalized the slip condition to arbitrary surfaces. However, this correction only affects the already empirically-determined slip length, thus the form of the boundary condition remains unchanged, while $a \approx 0.1$ is in good agreement with most experiments (Beavers et al., 1970). Zhang and Prosperetti (2009) provided further evidence for the slip boundary condition via pore-scale direct numerical simulations of a two-dimensional channel flow. A more detailed discussion of the history and mathematical foundations of the partial slip boundary condition can be found in (Nield & Bejan, 2013; Bottaro, 2019). Now, define the dimensionless quantity $\phi = \ell_{\text{slip}}/h_0$ as the slip coefficient. For the typical dimensions of a hydraulically-driven fracture, we estimate the dimensionless parameters values in Table 1.

To address the issue that fracture walls in the subsurface are themselves porous media, Mohais et al. (2011, 2012) employed the Beavers–Joseph boundary condition to solve for the flow in, and obtain a correction for the conductivity $\mathcal{K}$ of, uniform-depth fractures with permeable walls. So far, however, a theory for the conductivity of variable-depth fractures with porous walls (the most common case in the subsurface) is lacking. This study aims to fill this knowledge gap. Importantly, we also validate our proposed model for $\mathcal{K}$ against direct numerical simulations using a custom solver built on OpenFOAM® (Weller et al.,

1998; The OpenFOAM Foundation Ltd, 2020). We provide an implementation of the *semi-implicit method for pressure-linked equations* (SIMPLE) (see, e.g., Moukalled et al., 2016, Ch. 15) algorithm for the Navier–Stokes equations subject to the tensorial form of the Beavers–Joseph–Saffman (BJS) boundary condition.

2 Methods: Mathematical analysis and derivation of the conductivity

2.1 Governing equations

The flow geometry and notation are shown in Fig. 1. An incompressible Newtonian fluid of density ρ and dynamic viscosity μ fills the gap. The fracture is long and thin, which justifies taking $h(x)$ to be a linear function (Nicholl et al., 1999). Alternatively, one is allowed to substitute $\alpha = \alpha(x)$ in the results below if $dh/dx \neq const.$, as long as $\max_x \alpha(x)$ satisfies the original smallness assumption (Zimmerman & Bodvarsson, 1996; Wang et al., 2019). Let U_0 be the average inlet velocity at the inlet ($x = 0$), which serves as the scale for the horizontal velocity $u(x, z)$ in the fracture. The flow is assumed to be 2D, i.e., the fracture is infinite in the transverse y-direction. Then, conservation of mass requires that the scale for the vertical velocity $v(x, z)$ be $V_0 = U_0 h_0/L = \epsilon U_0$ (Conlisk, 2012, Sec. 4.9).

Now, we define the dimensionless (starred) variables

$$x^* = x/L, \quad z^* = z/h_0, \quad h^*(x^*) = h(x)/h_0, \quad u^*(x^*, z^*) = u(x, z)/U_0,$$
$$v^*(x^*, z^*) = v(x, z)/V_0, \quad p^*(x^*, z^*) = \epsilon h_0 p(x, z)/(\mu U_0), \quad \mathcal{K}^*(x^*) = \mathcal{K}(x)/h_0^2, \quad (1)$$

where $Re = \rho U_0 h_0/\mu$ is the Reynolds number and $\tilde{Re} = \epsilon Re$ is a reduced Reynolds number (Zimmerman & Bodvarsson, 1996). Then, the dimensionless conservation of mass and momentum equations are

$$\frac{\partial u^*}{\partial x^*} + \frac{\partial v^*}{\partial z^*} = 0, \quad (2a)$$

$$\tilde{Re}\left(u^*\frac{\partial u^*}{\partial x^*} + v^*\frac{\partial u^*}{\partial z^*}\right) = -\frac{\partial p^*}{\partial x^*} + \epsilon^2\frac{\partial^2 u^*}{\partial x^{*2}} + \frac{\partial^2 u^*}{\partial z^{*2}}, \quad (2b)$$

$$\epsilon^2\tilde{Re}\left(u^*\frac{\partial v^*}{\partial x^*} + v^*\frac{\partial v^*}{\partial z^*}\right) = -\frac{\partial p^*}{\partial z^*} + \epsilon^4\frac{\partial^2 v^*}{\partial x^{*2}} + \epsilon^2\frac{\partial^2 v^*}{\partial z^{*2}}, \quad (2c)$$

subject to the following boundary conditions (BCs):

$$\text{symmetry at } z^* = 0: \qquad \frac{\partial u^*}{\partial z^*} = 0 \qquad \text{and} \qquad v^* = 0; \quad (3a)$$

$$\text{partial slip at } z^* = h^*: \qquad u^* = -\phi\frac{\partial u^*}{\partial z^*}, \quad (3b)$$

where ϕ is the slip coefficient, and $h^* = h^*(x^*) = 1 + \alpha x^*/\epsilon$. Observe that, here, we can introduce $\delta = \alpha/\epsilon = [h(L) - h(0)]/h_0 = \Delta h/h_0$, which is the percent change of $h(x)$ over the typical fracture variation length L, so that $h^*(x^*) = 1 + \delta x^*$. The assumption of *slow variation* dictates that $\delta \ll 1$, while the assumption of *lubrication* (small aspect ration) dictates that $\epsilon = h_0/L \ll 1$ (see also Conlisk, 2012; Zimmerman & Bodvarsson, 1996). These two assumptions are independent and lead to $\alpha = \epsilon\delta \lll 1$, which is typical of fractures, as discussed in Sec. 1.

The BC in Eq. (3a) is the centerline symmetry condition, while the BC in Eq. (3b) comes from the BJS partial slip BC (Beavers & Joseph, 1967; Beavers et al., 1970; Saffman, 1971; Layton et al., 2002; Jäger & Mikelić, 2000) on the permeable wall (see Supporting Information Text S1 for details). Importantly, the BJS BC allows us to solve for the flow in the fracture without solving for the flow in the surround porous medium.

2.2 Perturbation solution for the velocity profile

Following the standard procedure of a regular perturbation expansion (Holmes, 2013), the velocity field is expanded as $u^* = u_0^* + \tilde{Re}\, u_1^* + \cdots$ and $v^* = v_0^* + \tilde{Re}\, v_1^* + \cdots$ ($\tilde{Re} \ll 1$). Then, we find the horizontal velocity at the leading order (see Supporting Information Text S1 for details):

$$u_0^*(x^*, z^*) = \left(\frac{h^{*2} - z^{*2}}{2} + \phi h^*\right)\left(-\frac{dp^*}{dx^*}\right). \tag{4}$$

Since the flow is in the direction of positive x^*, $dp^*/dx^* < 0$. Then, the leading-order depth-averaged velocity is

$$\langle u_0^* \rangle(x^*) = \frac{1}{h^*(x^*)} \int_0^{h^*(x^*)} u_0^*(x^*, z^*)\, dz^* = \frac{3\phi h^* + h^{*2}}{3}\left(-\frac{dp^*}{dx^*}\right). \tag{5}$$

And, the vertical velocity at the leading order is

$$v_0^*(x^*, z^*) = (h^* + \phi)\frac{dh^*}{dx^*} z^* \frac{dp^*}{dx^*} - \left(\frac{z^{*2}}{6} - \frac{h^{*2}}{2} - \phi h^*\right) z^* \frac{d^2 p^*}{dx^{*2}}. \tag{6}$$

At the next order in $\tilde{Re}$, we find the depth-averaged velocity's correction:

$$\langle u_1^* \rangle(x^*) = \left(\frac{3}{35}h^{*2} + \frac{\phi}{3}h^* + \frac{\phi^2}{3}\right) h^{*4} \left(-\frac{dp^*}{dx^*}\right) \frac{d^2 p^*}{dx^{*2}} - \left(\frac{h^*}{5} + \frac{\phi}{3}\right) h^{*3}(h^* + \phi) \frac{1}{\epsilon} \frac{dh^*}{dx^*} \left(\frac{dp^*}{dx^*}\right)^2. \tag{7}$$

For the present purposes, it is not necessary to write out u_1^* and v_1^* but they can be calculated (see Supporting Information Text S1).

2.3 Equivalent Darcy's law and the hydraulic conductivity

To obtain the conductivity $\mathcal{K}$ in a shaped fracture with porous walls, we must put the flow field thus obtained into the form of a Darcy-like law, i.e., $\langle u^* \rangle \propto -dp^*/dx^*$, with the proportionality factor being the sought-after result. To this end, combining Eqs. (5) and (7) we obtain the "full" depth-average horizontal velocity up to $\mathcal{O}(\tilde{Re})$: $\langle u^* \rangle = \langle u_0^* \rangle + \tilde{Re} \langle u_1^* \rangle$. However, at this point, the pressure distribution $p^*(x^*)$ is still *unknown*. To close the problem, we need another constraint. Mohais et al. (2012) provided one solution by assuming a *constant* permeation velocity v_w in a parallel fracture ($\alpha = dh^*/dx^* = 0$, $h^* = 1$), i.e., $v_0|_{z=\pm h_0} = \pm v_w$. We could apply this BC here too (see Supporting Information Text S1), however, as discussed in Sec. 1, the assumption of a constant v_w is not suitable for shaped fractures, due to the flow-wise x^*-variation of the aperture. Instead, to close the problem, we impose the full flux onto the leading-order depth-averaged velocity, i.e., we set $\langle u_0^* \rangle = 1$. Thus, v_w^* will *not* be constant and will be self-consistently determined as a function of dp^*/dx^*. Another modeling approach is to set the wall-normal velocity via the local pressure, as in filtration problems (Tilton et al., 2012; Herterich et al., 2015), however this approach is beyond the scope of the present study focused on porous media flows.

Applying the constraint $\langle u_0^* \rangle = 1$ to Eq. (5), we compute dp^*/dx^* and d^2p^*/dx^{*2} (see Supporting Information Text S1). Substituting the latter results into Eq. (7) and putting it all together,

$$\langle u^* \rangle = -\mathcal{K}^* \frac{dp^*}{dx^*}, \qquad \mathcal{K}^* = \mathcal{K}^*(x^*) = \left[\frac{3\phi h^* + h^{*2}}{3} - \tilde{Re}\frac{h^{*3}(28\phi^2 + 22\phi h^* + 3h^{*2})\delta}{35(3\phi + h^*)^2}\right], \tag{8}$$

which is already in the form of Darcy's law. Finally, Eq. (8) can be put in dimensional form:

$$\langle u \rangle = -\frac{\mathcal{K}}{\mu}\frac{\partial p}{\partial x}, \qquad \mathcal{K} = \frac{h_0^2}{3} C, \tag{9}$$

where we have defined the dimensionless function

$$C = C(x) = \left[3\phi h^* + h^{*2} - 3\tilde{Re}\frac{h^{*3}(28\phi^2 + 22\phi h^* + 3h^{*2})\delta}{35(3\phi + h^*)^2}\right]$$
$$= \underbrace{1}_{\text{(I)}} + \underbrace{3\phi}_{\text{(II)}} + \underbrace{\left[(2+3\phi)\frac{x}{L} - 3\tilde{Re}\,\frac{3 + 22\phi + 28\phi^2}{35(3\phi+1)^2}\right]}_{\text{(III)}}\delta + \mathcal{O}\left(\delta^2\right) \tag{10}$$

to represent the "correction" to the hydraulic conductivity of the fracture. As discussed in Sec. 1, typical fractures are long and shallow ($\epsilon \ll 1$), and the slopes of the wall variation are even smaller ($\alpha = \epsilon\delta \lll 1$), thus we expanded a number of terms in Eq. (10) into Taylor series and kept only terms up to $\mathcal{O}(\delta)$ to highlight the key physical effects of shape variation in a fracture with permeable walls.

The function C accounts for wall permeation through the BJS slip coefficient $\phi = \sqrt{k_w}/(ah_0)$, the shape of the fracture through the slope $\alpha = dh/dx$ and aspect ratio $\epsilon = h_0/L$, and weak inertia through the reduced Reynolds number $\tilde{Re} = \rho U_0 h_0^2/(\mu L)$. The first term (I) on the right-hand side of Eq. (10) corresponds to the classic conductivity calculated by the Hele-Shaw analogy (Bear, 1972); the second term (II) comes from wall permeation (Mohais et al., 2012); the third term (III), which is the novel contribution of our calculation, and is explicitly a function of the flow-wise coordinate x, is due to the *coupled* effect of geometry variation, fluid inertia, and wall permeation.

2.4 Wall permeation velocity

Substituting the expression for dp^*/dx^* into the vertical velocity from Eq. (6), and evaluating the result at $z^* = h^*$, we obtain the *a priori* unknown wall permeation velocity

$$v_w(x) = -V_0\frac{h(x)\delta}{3\phi h_0 + h(x)}. \tag{11}$$

Recall that $\alpha < 0$ ($\Rightarrow \delta < 0$), so $v_w > 0$, i.e., the velocity is *into* the wall. Observe that both v_w and the term (III) in C vanish for $\alpha = 0$ ($\Rightarrow \delta = 0$) (parallel walls) because, in this case, there is no driving force to push fluid into the porous walls. We have imposed the full volumetric flux onto the leading-order solution (see also Tavakol et al., 2017), and it must be conserved. Note $v_w \neq 0$ for $\phi = 0$ because there can still be fluid penetrating the wall in the normal direction even if there is no (tangential) slip. The permeation velocity for $\phi = 0$ is driven by the flow-wise contraction of the aperture (rather then being imposed *a priori* (Mohais et al., 2012)).

3 Results and Discussion

Figure 2 shows the flow profile generated from the perturbative solution from Sec. 2, for a fracture with linear depth variation. The streamlines highlight the 2D nature of the velocity field, as well as permeation through the fracture's top wall. The pressure does not vary with z^*, as required by the lubrication (small aspect ratio, $\epsilon \ll 1$) approximation.

Next, we validate our mathematical results against "full" Navier–Stokes direct numerical simulations (DNS) (Al-Yaarubi et al., 2013). We carried out DNS using the simpleFoam solver in OpenFOAM® ver. 7.0 (Weller et al., 1998; The OpenFOAM Foundation Ltd, 2020), an open-source library based on the *finite volume method* (Moukalled et al., 2016). The simulations (see Supporting Information Text S2 for description of the method) were performed using the Hele-Shaw cell geometry with varying depth along x from Fig. 1. Importantly, unlike previous computational studies on flow in fractures with permeable walls (Tian et al., 2018), we did *not* impose the wall (tangent and normal) velocities from the theory onto the simulations. The latter approach is akin to verification, while we seek validation (Roache, 1998) between theory and simulation. Instead, we imposed a tensorial slip

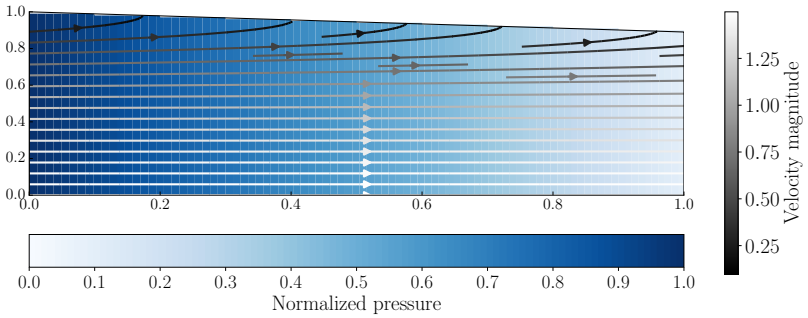

Figure 2. Illustration of the dimensionless analytical flow solution (Eqs. (4), (5) and (6)) obtained for the model shaped fracture with permeable walls. Only the top half ($z > 0$) is shown, for clarity. Background color denotes pressure, and curves are streamlines shaded by velocity magnitude. Here, $\alpha = -10^{-3}$, $\epsilon = 0.01$, $\tilde{Re} = 0.01$, $\phi = 10^{-3}$.

condition on the tangential velocity (the BJS BC) coupled with a normal pressure flux BC, to allow the simulation to self-consistently determine the flow (in particular, the unknown wall permeation velocity) and pressure profiles.

The DNSs provide the 2D velocity field $\big(u^*(x^*, z^*), v^*(x^*, z^*)\big)$ and the pressure distribution $p^*(x^*, z^*)$ (both scaled as in Eq. (1)). From these quantities, the volumetric flux across a vertical cross-section and the pressure gradient at a given x^* are computed, yielding $\langle u^*(x^*)\rangle$ and dp^*/dx^*. Their ratio, $\langle u^*\rangle/(-dp^*/dx^*)$ is to be compared to the theoretically predicted dimensionless conductivity $\mathcal{K}^*(x^*)$ from Eq. (8).

First, in Fig. 3, we show the velocity profiles across the midlength plane ($x^* = 0.5$) of fractures with different slopes. The simulation results agree well with theory. The zoomed-in inset in Fig. 3(a) highlights that u^* does not start from 0, but rather some finite value, as required by the BJC partial slip BC. For all α, $v^* = 0$ at the centerline ($z^* = 0$) as required by symmetry, then increases smoothly in absolute value towards the walls (Fig. 3(b)). Fluid enters into the surrounding porous medium and the wall permeation velocity $v_w^* = v^*|_{z^*=h^*}$ is self-consistently computed (shown in Supporting Information Fig. S7). The wall permeation velocity increases with $|\alpha|$ to maintain the imposed flux through these narrowing fractures. Meanwhile, for $\alpha = 0$, $v^* = 0$ for all z^*, i.e., there is no permeation into the porous medium, only slip at the fluid–solid interfaces ($z^* = \pm 1$).

To verify the derived analytical expression for the hydraulic conductivity in a shaped fracture, we compute $\mathcal{K}^*(x^*)$ in multiple angled fractures with permeable walls, based on typical reservoir properties summarized in Table 1. Figure 4(a) shows the predicted $\mathcal{K}^*$ (from theory) against the simulated $\mathcal{K}^*$ values along the fracture (multiple x^* for each) for multiple slope values α, and multiple slip coefficients ϕ, for fixed $\tilde{Re}$. In the same color family, the brightness of the color refers to the value of ϕ: the darker the color, the smaller ϕ is. The classical conductivity $\mathcal{K} = 1/3$ (i.e., for $\alpha = \phi = 0$) calculated from the Hele-Shaw analogy (Bear, 1972; Zimmerman & Bodvarsson, 1996) is shown by • (simulated) and — (predicted). All data points in Fig. 4(a) lie close to the line of slope 1, which means that the predicted conductivity (from theory) is in good agreement with the simulations. For $\phi > 10^{-3}$, the correlated trend continues, but in these cases the slip length is large and the single-domain simulation approach is not appropriate (the flow in the surrounding porous medium should be resolved as well to be able to impose suitable BCs numerically).

In Fig. 4(b), we plot the conductivity variation along the flow-wise (x^*) direction, a novel prediction of the present theory. By comparing the conductivity for the same α but

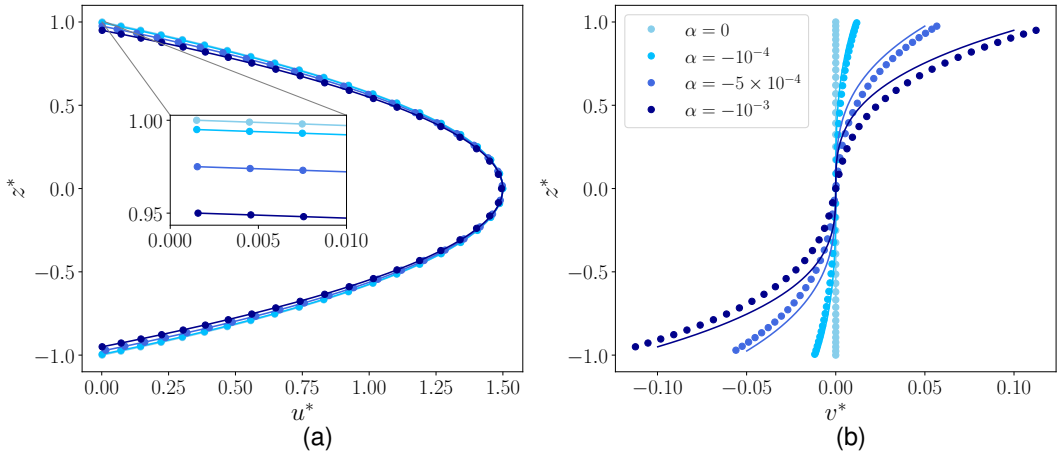

Figure 3. Velocity profiles versus fracture depth z^* at the mid-fracture plane $x^* = 0.5$, for $\phi = 5 \times 10^{-4}$ and $\tilde{Re} = 0.01$: (a) the horizontal component $u^*(x^*, z^*)$ (inset highlights the non-zero slip velocity at the wall); (b) the vertical component $v^*(x^*, z^*)$. Solid curves are the theoretical profiles from Eq. (6), and filled circles with the same colors are the corresponding simulation results. Colors represent different α values (see legend).

different ϕ, for example, $\alpha = -10^{-3}$ (the red color family), we observe that wall slip has only a weak effect on $\mathcal{K}^*$. By comparing the conductivity for different α (different color families), we observe that $\mathcal{K}^*$ decreases with x^*, which means that it becomes "harder" for the fluid to flow through the narrowing fractures. Of course this is expected on physical grounds, but this effect of α on $\mathcal{K}^*$ had not been quantified prior to this study. In particular, our results in Fig. 4 show that that even weak slopes have a much more significant impact on the conductivity, than wall slip due to the permeability of the walls. Likewise, the wall permeation velocity v_w^* has *not* been *a priori* specified, and is also a strong function of α (recall Sec. 2.4 and Supporting Information Fig. S7).

4 Conclusions and Outlook

The contribution of this study is the mathematical expressions, Eqs. (9) and (10), that relate the fracture conductivity to the geometric and physical quantities, and which explicitly shows the coupling between the fracture shape (in terms of its wall angle), the permeability of the porous wall (in terms of the Beavers–Joseph–Saffman slip length), and the inertia of the fluid in the fracture (in terms of a Reynolds number). Additionally, unlike previous studies on fractures with permeable walls, we self-consistently determined the wall permeation velocity, Eq. (6), which is *a priori* unknown and is set by the balance of pressure forces pushing fluid into the walls, and the permeability of the surrounding matrix. From these results, we concluded that the coupling effect of geometric variation, wall permeation and inertia leads to a decreasing conductivity along a narrowing fracture. Importantly, what has not been appreciated in previous studies is that, among these factors, the geometric variation (specifically, the resistance to flow induced by the narrowing of a fracture) dominates the conductivity change, even for slow shape variation (small slopes). The theoretical predictions were validated against direct numerical simulation of the Navier–Stokes equations in a model Hele-Shaw geometry.

In future work, the analytical solutions derived could be used to improve systems-level (network) modelling of hydraulic fracturing and transport (Gostick et al., 2016), wherein simple modifications of Darcy's law are currently used to capture the geometric variation

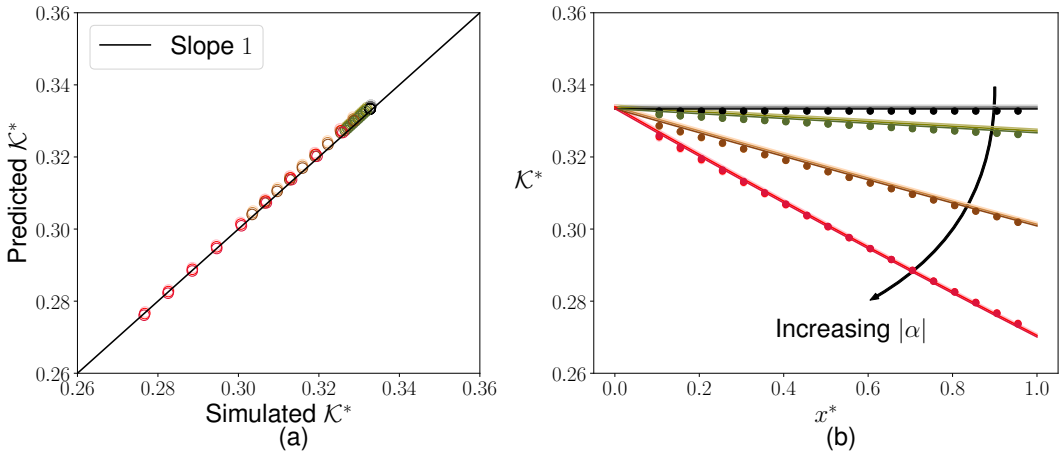

Figure 4. The conductivity $\mathcal{K}^*$ of shaped fractures, for different slip coefficients ϕ and geometry slopes α: (a) correlation plot of predicted $\mathcal{K}^*$ values versus simulated $\mathcal{K}^*$ values; (b) the variation of $\mathcal{K}^*(x^*)$ along the fracture length. Colors represent cases with different α and ϕ values: ●●●: $\alpha = 0$, $\phi \in \{0, 5 \times 10^{-4}, 10^{-3}\}$; ●●●: $\alpha = -10^{-4}$, $\phi \in \{0, 5 \times 10^{-4}, 10^{-3}\}$; ●●●: $\alpha = -5 \times 10^{-3}$, $\phi \in \{0, 5 \times 10^{-4}, 10^{-3}\}$; ●●●: $\alpha = -10^{-3}$, $\phi \in \{0, 5 \times 10^{-4}, 10^{-3}\}$. In (b), filled circles represent the simulation results, and solid curves of the same color represent the corresponding theoretical prediction Eq. (10) with $\tilde{Re} = 0.01$.

and wall permeability (Birdsell et al., 2015). Likewise, our hydraulic conductivity expression accounting for aperture variation and wall permeation could prove useful in modeling the alteration of fractures by precipitation and dissolution in geothermal systems (Chaudhuri et al., 2008). In this context, the OpenFOAM® solver developed could be adapted to account for solute non-Fickian transport and wall reactions (Municchi & Icardi, 2020). Our results could also guide the design of microfluidic analogues of porous media flows (Sinton, 2014) for emerging reservoir-on-a-chip technologies (Kumar Gunda et al., 2011) meant to emulate flow in geophysical reservoirs (Porter et al., 2015). Additionally, our solutions for the wall permeation velocity can be employed to estimate leakage in near-well operations, which can improve the accuracy of reservoir simulations (Dumkwu et al., 2012) and estimate the water content in low permeability layers (needed to establish the effectiveness of carbon dioxide sequestration (Gilmore et al., 2020)).

Data Availability Statement

The OpenFOAM® solver, example simulation configuration files, and post-processing scripts are freely available in this in-text data citation reference: Lu et al. (2020) [University of Illinois/NCSA Open Source License].

Acknowledgments

Acknowledgment is made to the donors of the American Chemical Society Petroleum Research Fund for support of this research under ACS PRF award # 57371-DNI9. I.C.C. is also affiliated with the Center for the Environment at Purdue University.

References

Al-Yaarubi, A. H., Pain, C. C., Grattoni, C. A., & Zimmerman, R. W. (2013). Navier-Stokes simulations of fluid flow through a rock fracture. In B. Faybishenko, P. A. Wither-

spoon, & J. Gale (Eds.), *Dynamics of fluids and transport in fractured rock* (Vol. 162, pp. 55–64). Washington, DC: American Geophysical Union. doi: 10.1029/162GM07

Barbati, A. C., Desroches, J., Robisson, A., & McKinley, G. H. (2016). Complex fluids and hydraulic fracturing. *Annu. Rev. Chem. Biomol. Eng.*, *7*, 415–453. doi: 10.1146/annurev-chembioeng-080615-033630

Bear, J. (1972). *Dynamics of Fluids in Porous Media*. New York, NY: American Elsevier Publishing Company, Inc.

Beavers, G. S., & Joseph, D. D. (1967). Boundary conditions at a naturally permeable wall. *J. Fluid Mech.*, *30*, 197–207. doi: 10.1017/S0022112067001375

Beavers, G. S., Sparrow, E. M., & Magnuson, R. A. (1970). Experiments on coupled parallel flows in a channel and a bounding porous medium. *ASME J. Basic Eng.*, *92*, 843–848. doi: 10.1115/1.3425155

Berkowitz, B. (1989). Boundary conditions along permeable fracture walls: Influence on flow and conductivity. *Water Res. Res.*, *25*, 1919–1922. doi: 10.1029/WR025i008p01919

Berman, A. S. (1953). Laminar flow in channels with porous walls. *J. Appl. Phys.*, *24*, 1232–1235. doi: 10.1063/1.1721476

Birdsell, D. T., Rajaram, H., Dempsey, D., & Viswanathan, H. S. (2015). Hydraulic fracturing fluid migration in the subsurface: A review and expanded modeling results. *Water Res. Res.*, *51*, 7159–7188. doi: 10.1002/2015WR017810

Bottaro, A. (2019). Flow over natural or engineered surfaces: an adjoint homogenization perspective. *J. Fluid Mech.*, *877*, P1. doi: 10.1017/jfm.2019.607

Brady, J. F. (1984). Flow development in a porous channel and tube. *Phys. Fluids*, *27*, 1061. doi: 10.1063/1.864735

Brown, S. R. (1987). Fluid flow through rock joints: The effect of surface roughness. *J. Geophys. Res.*, *92*(B2), 1337–1347. doi: 10.1029/JB092iB02p01337

Chaudhuri, A., Rajaram, H., & Viswanathan, H. (2008). Alteration of fractures by precipitation and dissolution in gradient reaction environments: Computational results and stochastic analysis. *Water Res. Res.*, *44*, W10410. doi: 10.1029/2008WR006982

Conlisk, A. T. (2012). *Essentials of Micro- and Nanofluidics with Applications to the Biological and Chemical Sciences*. New York, NY: Cambridge University Press.

Detournay, E. (2016). Mechanics of hydraulic fractures. *Annu. Rev. Fluid Mech.*, *48*, 311–339. doi: 10.1146/annurev-fluid-010814-014736

Dumkwu, F. A., Islam, A. W., & Carlson, E. S. (2012). Review of well models and assessment of their impacts on numerical reservoir simulation performance. *J. Petrol. Sci. Eng.*, *82-83*, 174–186. doi: 10.1016/j.petrol.2011.12.005

Garagash, D., & Detournay, E. (1999). The tip region of a fluid-driven fracture in an elastic medium. *ASME J. Appl. Mech.*, *67*, 183–192. doi: 10.1115/1.321162

Gilmore, K. A., Neufeld, J. A., & Bickle, M. J. (2020). CO2 dissolution trapping rates in heterogeneous porous media. *Geophys. Res. Lett.*, *47*, e2020GL087001. doi: 10.1029/2020GL087001

Gostick, J., Aghighi, M., Hinebaugh, J., Tranter, T., Hoeh, M. A., Day, H., ... Putz, A. (2016). OpenPNM: A pore network modeling package. *Comput. Sci. Eng.*, *18*(4), 60–74. doi: 10.1109/MCSE.2016.49

Grotberg, J. B. (1984). Volume-cycled oscillatory flow in a tapered channel. *J. Fluid Mech.*, *141*, 249–264. doi: 10.1017/S0022112084000823

Herterich, J. G., Vella, D., Field, R. W., Hankins, N. P., & Griffiths, I. M. (2015). Tailoring wall permeabilities for enhanced filtration. *Phys. Fluids*, *27*, 053102. doi: 10.1063/1.4919658

Holmes, M. H. (2013). *Introduction to Perturbation Methods* (2nd ed., Vol. 20). New York, NY: Springer Science+Business Media. doi: 10.1007/978-1-4614-5477-9

Hyman, J. D., Jiménez-Martínez, J., Viswanathan, H. S., Carey, J. W., Porter, M. L., Rougier, E., ... Makedonska, N. (2016). Understanding hydraulic fracturing: a multi-scale problem. *Phil. Trans. R. Soc. A*, *374*, 20150426. doi: 10.1098/rsta.2015.0426

Iliev, O., Mikelić, A., & Popov, P. (2008). On upscaling certain flows in deformable porous media. *Multiscale Model. Simul.*, *7*, 93–123. doi: 10.1137/06067732X

Jäger, W., & Mikelić, A. (2000). On the interface boundary condition of Beavers, Joseph, and Saffman. *SIAM J. Appl. Math.*, *60*, 1111–1127. doi: 10.1137/S003613999833678X

Jin, Y., Dong, J., Zhang, X., Li, X., & Wu, Y. (2017). Scale and size effects on fluid flow through self-affine rough fractures. *Int. J. Heat Mass Transfer*, *105*, 443–451. doi: 10.1016/j.ijheatmasstransfer.2016.10.010

Karra, S., Makedonska, N., Viswanathan, H. S., Painter, S. L., & Hyman, J. D. (2015). Effect of advective flow in fractures and matrix diffusion on natural gas production. *Water Res. Res.*, *51*, 8646–8657. doi: 10.1002/2014WR016829

King, J. R., & Cox, S. M. (2001). Asymptotic analysis of the steady-state and time-dependent Berman problem. *J. Eng. Math.*, *39*, 87–130. doi: 10.1023/A:1004824527547

Kumar, A., Datta, S., & Kalyanasundaram, D. (2016). Permeability and effective slip in confined flows transverse to wall slippage patterns. *Phys. Fluids*, *28*, 082002. doi: 10.1063/1.4959184

Kumar Gunda, N. S., Bera, B., Karadimitriou, N. K., Mitra, S. K., & Hassanizadeh, S. M. (2011). Reservoir-on-a-Chip (ROC): A new paradigm in reservoir engineering. *Lab Chip*, *11*, 3785. doi: 10.1039/c1lc20556k

Layton, W. J., Schieweck, F., & Yotov, I. (2002). Coupling fluid flow with porous media flow. *SIAM J. Numer. Anal.*, *40*, 2195–2218. doi: 10.1137/S0036142901392766

Lu, D., Municchi, F., & Christov, I. C. (2020). *The Hydraulic Conductivity of Shaped Fractures With Permeable Walls.* Zenodo. doi: 10.5281/zenodo.3934416

McBride, J., & Aly Sergie, M. (2015). *Hydraulic Fracturing (Fracking)* (Tech. Rep.). Council on Foreign Relations. Retrieved from `https://www.cfr.org/backgrounder/hydraulic-fracturing-fracking`

Mohais, R., Xu, C., & Dowd, P. (2011). Fluid flow and heat transfer within a single horizontal fracture in an enhanced geothermal system. *ASME J. Heat Transfer*, *133*, 112603. doi: 10.1115/1.4004369

Mohais, R., Xu, C., Dowd, P. A., & Hand, M. (2012). Permeability correction factor for fractures with permeable walls. *Geophys. Res. Lett.*, *39*, L03403. doi: 10.1029/2011GL050519

Mohais, R., Xu, C., Dowd, P. A., & Hand, M. (2016). Enhanced Geothermal Systems. In J. H. Lehr, J. Keeley, & T. B. Kingery (Eds.), *Alternative energy and shale gas encyclopedia* (pp. 265–289). Hoboken, NJ: Wiley. doi: 10.1002/9781119066354.ch27

Moukalled, F., Mangani, L., & Darwish, M. (2016). *The Finite Volume Method in Computational Fluid Dynamics: An Advanced Introduction with OpenFOAM® and Matlab.* Cham, Switzerland: Springer International Publishing. doi: 10.1007/978-3-319-16874-6

Municchi, F., & Icardi, M. (2020). Macroscopic models for filtration and heterogeneous reactions in porous media. *Adv. Water. Res.*, *141*, 103605. doi: 10.1016/j.advwatres.2020.103605

Nicholl, M. J., Rajaram, H., Glass, R. J., & Detwiler, R. (1999). Saturated flow in a single fracture: evaluation of the Reynolds Equation in measured aperture fields. *Water Res. Res.*, *35*, 3361–3373. doi: 10.1029/1999WR900241

Nield, D. A., & Bejan, A. (2013). Mechanics of Fluid Flow Through a Porous Medium. In *Convection in porous media* (4th ed., pp. 1–29). New York, NY: Springer Science+Business Media. doi: 10.1007/978-1-4614-5541-7{_}1

Olasolo, P., Juárez, M. C., Morales, M. P., D'Amico, S., & Liarte, I. A. (2016). Enhanced geothermal systems (EGS): A review. *Renew. Sust. Energ. Rev.*, *56*, 133–144. doi: 10.1016/j.rser.2015.11.031

Osiptsov, A. A. (2017). Fluid mechanics of hydraulic fracturing: A review. *J. Petrol. Sci. Eng.*, *156*, 513–535. doi: 10.1016/j.petrol.2017.05.019

Patzek, T. W., Male, F., & Marder, M. (2013). Gas production in the Barnett Shale obeys a simple scaling theory. *Proc. Natl Acad. Sci. USA*, *110*, 19731–19736. doi: 10.1073/pnas.1313380110

Phillips, O. M. (1991). *Flow and Reactions in Permeable Rocks.* New York, NY: Cambridge University Press.

Porter, M. L., Jiménez-Martinez, J., Martinez, R., McCulloch, Q., Carey, J. W., & Viswanathan, H. S. (2015). Geo-material microfluidics at reservoir conditions for subsurface energy resource applications. *Lab Chip*, *15*, 4044–4053. doi: 10.1039/C5LC00704F

Rahman, M. M., & Rahman, M. K. (2010). A review of hydraulic fracture models and development of an improved pseudo-3D model for stimulating tight oil/gas sand. *Energy Sources Part A-Recovery Util. Environ. Eff.*, *32*, 1416–1436. doi: 10.1080/15567030903060523

Rassenfoss, S. (2015). What Do Fractures Look Like? A Picture Says A Lot, Even When It is Wrong. *J. Petrol. Tech.*, *67*(5), 60–68. doi: 10.2118/0515-0060-JPT

Roache, P. J. (1998). *Verification and Validation in Computational Science and Engineering.* Socorro, New Mexico: Hermosa Publishers.

Rosti, M. E., Pramanik, S., Brandt, L., & Mitra, D. (2020). The breakdown of Darcy's law in a soft porous material. *Soft Matter*, *16*, 939–944. doi: 10.1039/C9SM01678C

Saffman, P. G. (1971). On the boundary condition at the surface of a porous medium. *Stud. Appl. Math.*, *50*, 93–101. doi: 10.1002/sapm197150293

Sellars, J. R. (1955). Laminar flow in channels with porous walls at high suction Reynolds numbers. *J. Appl. Phys.*, *26*, 489–490. doi: 10.1063/1.1722024

Sinton, D. (2014). Energy: the microfluidic frontier. *Lab Chip*, *14*, 3127–3134. doi: 10.1039/C4LC00267A

Tavakol, B., Froehlicher, G., Stone, H. A., & Holmes, D. P. (2017). Extended lubrication theory: Improved estimates of flow in channels with variable geometry. *Proc. R. Soc. A*, *473*, 20170234. doi: 10.1098/rspa.2017.0234

Taylor, G. I. (1971). A model for the boundary condition of a porous material. Part 1. *J. Fluid Mech.*, *49*, 319–326. doi: 10.1017/S0022112071002088

Terrill, R. M., & Shrestha, G. M. (1964). Laminar flow through parallel and uniformly porous walls of different permeability. *Z. Angew. Math. Phys. (ZAMP)*, *16*, 470–482. doi: 10.1007/BF01593923

The OpenFOAM Foundation Ltd. (2020). *OpenFOAM.* Retrieved from `http://www.openfoam.org`

Tian, Z. F., Xu, C., & Dowd, P. A. (2018). Numerical simulation of flows in a channel with impermeable and permeable walls using finite volume methods. In N. Narayanan, B. Mohanadhas, & V. Mangottiri (Eds.), *Flow and transport in subsurface environment* (pp. 119–140). Singapore: Springer. doi: 10.1007/978-981-10-8773-8{_}4

Tilton, N., Martinand, D., Serre, E., & Lueptow, R. M. (2012). Incorporating Darcy's law for pure solvent flow through porous tubes: Asymptotic solution and numerical simulations. *AIChE J.*, *58*, 2030–2044. doi: 10.1002/aic.13823

Van Dyke, M. (1987). Slow variations in continuum mechanics. *Adv. Appl. Mech.*, *25*, 1–45. doi: 10.1016/S0065-2156(08)70276-X

van Golf-Racht, T. D. (1982). *Fundamentals of Fractured Reservoir Engineering* (1st ed., Vol. 12). Amsterdam, The Netherlands: Elsevier Scientific Publishing Company. doi: 10.1016/S0376-7361(08)70330-3

Vincent, M. C. (2002). Proving It - A Review of 80 Published Field Studies Demonstrating the Importance of Increased Fracture Conductivity. In *Proc. spe annual technical conference and exhibition.* San Antonio, Texas: Society of Petroleum Engineers. doi: 10.2118/77675-MS

Wang, Z., Xu, C., & Dowd, P. (2019, 5). Perturbation Solutions for Flow in a Slowly Varying Fracture and the Estimation of Its Transmissivity. *Transport in Porous Media*, *128*(1), 97–121. Retrieved from `http://link.springer.com/10.1007/s11242-019-01237-7` doi: 10.1007/s11242-019-01237-7

Weller, H. G., Tabor, G., Fureby, C., & Jasak, H. (1998). A tensorial approach to computational continuum mechanics using object-oriented techniques. *Comput. Phys.*, *12*, 620–631. doi: 10.1063/1.168744

Witherspoon, P. A., Wang, J. S. Y., Iwai, K., & Gale, J. E. (1980). Validity of Cubic Law for fluid flow in a deformable rock fracture. *Water Res. Res.*, *16*, 1016–1024. doi: 10.1029/WR016i006p01016

Yew, C. H., & Weng, X. (2015). *Mechanics of Hydraulic Fracturing* (2nd ed.). Waltham, MA: Gulf Professional Publishing. doi: 10.1016/C2013-0-12927-3

Zhang, Q., & Prosperetti, A. (2009). Pressure-driven flow in a two-dimensional channel with porous walls. *J. Fluid Mech.*, *631*, 1–21. doi: 10.1017/S0022112009005837

Zimmerman, R. W., & Bodvarsson, G. S. (1996). Hydraulic conductivity of rock fractures. *Transp. Porous Med.*, *23*, 1–30. doi: 10.1007/BF00145263

Supporting Information for "The Hydraulic Conductivity of a Shaped Fracture With Permeable Walls"

DOI: 10.1002/xxx

Daihui Lu[1], Federico Municchi[2], and Ivan C. Christov[1]

[1]School of Mechanical Engineering, Purdue University, West Lafayette, Indiana 47907, USA

[2]School of Mathematical Sciences, The University of Nottingham, University Park, Nottingham, NG7 2RD, UK

Contents of this file

Introduction

The supporting information consists of two texts S1 and S2, seven figures S1 to S7, and a table S1.

Corresponding author: I. C. Christov, School of Mechanical Engineering, Purdue University, West Lafayette, Indiana 47907, USA. (christov@purdue.edu)

Supporting Information Text S1 provides the steps in the derivation of the hydraulic conductivity presented and discussed in the main text. These steps are included for completeness and to aid a reader in following the mathematical derivation.

Supporting Information Text S2 describes the OpenFOAM® solver methodology for generating the direct numerical simulation data reported in the main text. Text S2 includes ancillary details about the verification of the simulations (grid independence tests) and post-processing of the simulation data. Toward these ends, Fig. S1 through S5 are referenced as part of Text S2.

The OpenFOAM® solver and post-processing scripts are freely available at the repository `https://github.com/daihui-lu/HydraulicConductivityofShapedFractures`, per the AGU data policy and as stated in the "Data Availability Statement" of the main text.

Figures S6 and S7 are complementary representations of data and information discussed in the main text. They are provided for completeness but are not essential to the conclusions in the main text.

Text S1.

The Beavers–Joseph–Saffman (BJS) (Beavers & Joseph, 1967; Saffman, 1971) partial slip boundary condition (BC) on the permeable wall is

$$u^* = -\phi\left(\frac{\partial u^*}{\partial z^*} + \epsilon^2\frac{\partial v^*}{\partial x^*}\right) = -\phi\frac{\partial u^*}{\partial z^*} + \mathcal{O}(\epsilon^2) \qquad \text{at} \qquad z^* = \pm h^*(x^*). \tag{SI.1}$$

The slip coefficient ϕ, which is a dimensionless slip length (i.e., $\phi = \ell_{\text{slip}}/h_0$), is an empirically-measurable quantity that accounts for the actual flow into the porous walls and their permeability, as discussed in the Introduction of the main text.

Let $\tilde{Re} = \epsilon Re$ be finite as $\epsilon \to 0$. Then, upon taking the limit $\epsilon \to 0$ of Eqs. (2) from the main text, Eq. (2a) remains unchanged, and Eqs. (2b) and (2c) become

$$\tilde{Re}\, u^*\frac{\partial u^*}{\partial x^*} + \tilde{Re}\, v^*\frac{\partial u^*}{\partial z^*} = -\frac{\partial p^*}{\partial x^*} + \frac{\partial^2 u^*}{\partial z^{*2}}, \tag{SI.2a}$$

$$0 = -\frac{\partial p^*}{\partial z^*}. \tag{SI.2b}$$

Now, assume a regular perturbation expansion in $\tilde{Re} \ll 1$. The velocity field is expanded as

$$u^* = u_0^* + \tilde{Re}\, u_1^* + \cdots, \tag{SI.3a}$$

$$v^* = v_0^* + \tilde{Re}\, v_1^* + \cdots. \tag{SI.3b}$$

Substituting Eqs. (SI.3) into Eqs. (SI.2) and neglecting $\mathcal{O}(\tilde{Re})$ and higher-order terms, we obtain the leading-order momentum equations:

$$0 = -\frac{\partial p^*}{\partial x^*} + \frac{\partial^2 u_0^*}{\partial z^{*2}}, \tag{SI.4a}$$

$$0 = -\frac{\partial p^*}{\partial z^*}, \tag{SI.4b}$$

subject to the boundary conditions

$$\left.\frac{\partial u_0^*}{\partial z^*}\right|_{z^*=0} = 0, \quad v_0^*|_{z^*=0} = 0 \quad \text{and} \quad u_0^*|_{z^*=h^*} = -\phi \left.\frac{\partial u^*}{\partial z^*}\right|_{z^*=h^*}. \tag{SI.5}$$

Recall that, by symmetry, we are only solving for the profile in the top half of the fracture. Therefore, the leading-order solution for the horizontal velocity has the form

$$u_0^*(x^*, z^*) = \frac{1}{2}\frac{dp^*}{dx^*} z^{*2} + \mathfrak{C}_1(x^*) z^* + \mathfrak{C}_2(x^*), \tag{SI.6}$$

where $\mathfrak{C}_1$ and $\mathfrak{C}_2$ are arbitrary (integration) functions of x^*. Since p^* is independent of z^* by Eq. (SI.4b), henceforth we write $\partial p^*/\partial x^* = dp^*/dx^*$. Imposing the boundary conditions (SI.5) onto Eq. (SI.6), we obtain

$$u_0^*(x^*, z^*) = \left(\frac{h^{*2} - z^{*2}}{2} + \phi h^*\right)\left(-\frac{dp^*}{dx^*}\right). \tag{SI.7}$$

Since the flow is in the direction of positive x^*, $dp^*/dx^* < 0$, so we choose to associate a negative sign with this term in some equations, for clarity, as is standard in the fluid mechanics literature. Then, the leading-order depth-averaged velocity is

$$\langle u_0^* \rangle(x^*) = \frac{1}{h^*(x^*)} \int_0^{h^*(x^*)} u_0^*(x^*, z^*)\, dz^* = \frac{3\phi h^*(x^*) + h^*(x^*)^2}{3}\left(-\frac{dp^*}{dx^*}\right). \tag{SI.8}$$

Next, we determine the leading-order vertical velocity. From the conservation of mass equation,

$$\frac{\partial u^*}{\partial x^*} + \frac{\partial v^*}{\partial z^*} = 0, \tag{SI.9}$$

we deduce that

$$\frac{\partial v_0^*}{\partial z^*} = -\frac{\partial u_0^*}{\partial x^*} = \left(h^*\frac{dh^*}{dx} + \phi\frac{dh^*}{dx}\right)\frac{dp^*}{dx^*} - \left(\frac{z^{*2} - h^{*2}}{2} - \phi h^*\right)\frac{d^2p^*}{dx^{*2}}. \tag{SI.10}$$

Now, integrating both sides of Eq. (SI.10) from 0 to an arbitrary z^*, and using the second boundary condition in Eq. (SI.5), we find that the vertical velocity is

$$v_0^*(x^*, z^*) = \left(h^* \frac{dh^*}{dx} + \phi \frac{dh^*}{dx}\right) z^* \frac{dp^*}{dx^*} - \left(\frac{z^{*3}}{6} - \frac{h^{*2} z^*}{2} - \phi h^* z^*\right) \frac{d^2 p^*}{dx^{*2}}. \tag{SI.11}$$

From Eqs. (SI.2), we obtain the first-order perturbation equation:

$$u_0^* \frac{\partial u_0^*}{\partial x^*} + v_0^* \frac{\partial u_0^*}{\partial z^*} = \frac{\partial^2 u_1^*}{\partial z^{*2}}. \tag{SI.12}$$

Substituting the $\mathcal{O}(1)$ solution from Eq. (SI.7) above into Eq. (SI.12), we obtain

$$\frac{\partial^2 u_1^*}{\partial z^{*2}} = \left[\left(\frac{h^{*2}}{2} + \phi h^*\right)^2 + \frac{z^{*4}}{12}\right] \frac{dp^*}{dx^*} \frac{d^2 p^*}{dx^{*2}} + \left(\frac{h^{*2} + z^{*2}}{2} + \phi h^*\right) (h^* + \phi) \frac{\alpha}{\epsilon} \left(\frac{dp^*}{dx^*}\right)^2, \tag{SI.13}$$

subject to homogeneous BCs:

$$\left.\frac{\partial u_1^*}{\partial z^*}\right|_{z^*=0} = 0 \quad \text{and} \quad u_1^*|_{z^*=h^*} = 0. \tag{SI.14}$$

Integrating both sides of Eq. (SI.13) from 0 to an arbitrary z^*, and substituting the boundary conditions from Eq. (SI.14), we obtain the first-order inertial correction to the horizontal velocity component:

$$\begin{aligned} u_1^*(x^*, y^*) = &\left[\left(\frac{h^{*2}}{2} + \phi h^*\right)^2 \frac{z^{*2} - h^{*2}}{2} + \frac{1}{360}\left(z^{*6} - h^{*6}\right)\right] \frac{dp^*}{dx^*} \frac{d^2 p^*}{dx^{*2}} \\ &+ \left[\left(\frac{h^{*2}}{2} + \phi h^*\right) \frac{z^{*2} - h^{*2}}{2} + \frac{z^{*4} - h^{*4}}{24}\right] (h^* + \phi) \frac{\alpha}{\epsilon} \left(\frac{dp^*}{dx^*}\right)^2. \end{aligned} \tag{SI.15}$$

From the latter, we find the depth-averaged velocity correction:

$$\begin{aligned} \langle u_1^* \rangle &= \frac{1}{h^*(x^*)} \int_0^{h^*(x^*)} u_1^*(x^*, z^*)\, dz^* \\ &= \left(\frac{3}{35} h^{*6} + \frac{1}{3} \phi h^{*5} + \frac{\phi^2}{3} h^{*4}\right) \left(-\frac{dp^*}{dx^*}\right) \frac{d^2 p^*}{dx^{*2}} - \left(\frac{1}{5} h^{*4} + \frac{1}{3} \phi h^{*3}\right) (h^* + \phi) \frac{\alpha}{\epsilon} \left(\frac{dp^*}{dx^*}\right)^2. \end{aligned} \tag{SI.16}$$

To close the problem, we need another constraint. Mohais, Xu, Dowd, and Hand (2012) provided one solution by assuming a *constant* permeation velocity v_w in a parallel fracture

($\alpha = 0$, $h^* = 1$), i.e., $v_0|_{z=\pm h} = \pm v_w$ ($v_0^*|_{z^*=\pm 1} = \pm 1$). If we apply this constraint to the above analysis, the dimensionless average horizontal velocity becomes

$$\begin{aligned}\langle u^* \rangle &= \left[\frac{3\phi+1}{3} + \tilde{Re}\left(\frac{3}{35} + \frac{1}{3}\phi + \frac{\phi^2}{3}\right)\frac{3}{3\phi+1}\right]\left(-\frac{dp^*}{dx^*}\right) \\ &= \left(\frac{3\phi+1}{3}\right)\left[1 + \tilde{Re}\left(\frac{3}{35} + \frac{1}{3}\phi + \frac{\phi^2}{3}\right)\frac{9}{(3\phi+1)^2}\right]\left(-\frac{dp^*}{dx^*}\right).\end{aligned} \tag{SI.17}$$

This solution differs from (Mohais et al., 2012) in that the we have expanded only the velocity u^* in powers of $\tilde{Re}$, while Mohais et al. (2012) expanded p^* as well and obtained (using our notation):

$$-\frac{dp^*}{dx^*} = \langle u^* \rangle \left\{\frac{3}{1+3\phi} - \tilde{Re}\left[\frac{9(7\phi+1)}{140(1+3\phi)^3} + \left(\frac{3+6\phi}{2+6\phi}\right)^2\right]\right\}. \tag{SI.18}$$

To the leading order in $\tilde{Re}$, we may use the Taylor series $(1-\xi)^{-1} = 1 + \xi + \mathcal{O}(\xi^2)$ to rewrite (SI.18) as

$$\langle u^* \rangle = \left(\frac{3\phi+1}{3}\right)\left\{1 + \tilde{Re}\left[\frac{3(7\phi+1)}{140(3\phi+1)^2} + \frac{3(2\phi+1)^2}{4(3\phi+1)}\right]\right\}\left(-\frac{dp^*}{dx^*}\right). \tag{SI.19}$$

Despite the different expansion methods used to obtain Eqs. (SI.17) and (SI.19), the leading-order terms are the same, i.e., they both yield:

$$\langle u^* \rangle = \frac{1}{3}(1+3\phi)\left(1 + \frac{27}{35}\tilde{Re}\right)\left(-\frac{dp^*}{dx^*}\right) + \mathcal{O}(\tilde{Re}^2, \phi^2, \phi\tilde{Re}), \tag{SI.20}$$

meaning they are asymptotically equivalent at the leading order in $\phi \ll 1$ and $\tilde{Re} \ll 1$.

Now, however, the wall permeation velocity v_w (and its relation to the pressure gradient dp/dx) is not necessarily known *a priori*. To close the problem, we apply the flux constraint $\langle u_0^* \rangle = 1$ to Eq. (SI.8), and we obtain

$$\frac{dp^*}{dx^*} = -\frac{3}{3\phi h^*(x^*) + h^*(x^*)^2} \qquad \Rightarrow \qquad \frac{d^2p^*}{dx^{*2}} = \frac{(9\phi + 6h^*)\delta}{[3\phi h^*(x^*) + h^*(x^*)^2]^2}. \tag{SI.21}$$

Substituting the latter results into Eq. (SI.16) and suppressing the explicit notation that h^* is a function of x^*, we have

$$\langle u_1^* \rangle = \frac{h^{*3}(28\phi^{*2} + 22\phi h^* + 3h^{*2})\delta}{35(3\phi + h^*)^2} \frac{dp^*}{dx^*}. \tag{SI.22}$$

Finally, from Eqs. (SI.8) and (SI.22), $\langle u^* \rangle$ can be reconstituted into a Darcy's law, as shown in Eq. (8) in the main text and discussed therein.

Text S2.

The solution algorithm for the incompressible Navier–Stokes equations [Eqs. (2) in the main text] used in our direct numerical simulation (DNS) study is SIMPLE (*semi-implicit method for pressure-linked equations*) (see, e.g., Moukalled et al., 2016, Ch. 15). In this study, we set the tolerance for the pressure and velocity components' residuals to be 10^{-5} (see the example convergence plot in Fig. S1). The BCs applied in the simulation are summarized in the schematic in Fig. S2. In particular, note that the BJS BC (SI.1) is, mathematically, a Robin (or mixed-type) BC. However, within the iterative algorithm, we reformulated it as a Dirichlet boundary condition to enhance stability and ensure consistency of fluxes within the pressure iterations.

The BJS BC, as given in the computational paper by Layton, Schieweck, and Yotov (2002), is essentially a slip condition enforcing a specific value of the velocity field in the face-planar direction of the boundary cell. In this formulation, the condition does not alter the velocity normal to the porous walls.

In OpenFOAM® (Weller et al., 1998; The OpenFOAM Foundation Ltd, 2020) and, more generally, in the finite volume method (Moukalled et al., 2016), discretization is performed by summing all the contribution from the volumetric source terms (if present) and fluxes, looping over all the cell faces. In order to discretize generic differential equations without any specific knowledge of the form of the fluxes, OpenFOAM® requires that each flux is expressed in terms of a face value $\boldsymbol{u}_f$ and a face-normal gradient $(\nabla \boldsymbol{u})_f \cdot \boldsymbol{n}_f$, where f is a generic face and $\boldsymbol{n}_f$ is the vector normal to such face. Therefore, an explicit or implicit (i.e., matrix coefficients) expression for those two face-based fields is required.

Boundary faces are no exception. Thus, with reference to Fig. S3, it is necessary to provide expressions for $\boldsymbol{u}_b$ and $(\nabla \boldsymbol{u})_b \cdot \boldsymbol{n}$ that take into account the BJS BC. In vector form, the boundary condition reads:

$$\mathbf{T} \cdot \boldsymbol{u}_b = -\mathbf{T} \cdot \left(\ell \frac{\partial \boldsymbol{u}}{\partial n} \right)_b , \tag{SI.23}$$

where $\mathbf{T} = (\mathbf{I} - \boldsymbol{n}\boldsymbol{n})$ is the projector on the tangential plane, $\mathbf{I}$ is the identity operator, and $\ell = \ell_{\text{slip}}$ is the BJS slip length discussed in the main text.

However, a problem described by the Navier–Stokes equations with a BC of the type in Eq. (SI.23) is not well posed, since such condition only constrains the face-planar field. Therefore, it is necessary to specify a condition on the face-normal field. Since the BJS BC does not provide such a constrain, we assume that all the flow arriving normal to the boundary leaves the domain. This assumption corresponds to:

$$\boldsymbol{n} \cdot \left(\frac{\partial \boldsymbol{u}}{\partial n} \right)_b = 0 . \tag{SI.24}$$

In this sense, condition (SI.24) merely correspond to copying the value of the velocity field in the first cell. In fact, using a linear interpolation scheme one obtains:

$$\boldsymbol{n} \cdot \left(\frac{\partial \boldsymbol{u}}{\partial n} \right)_b \approx \frac{\boldsymbol{n} \cdot (\boldsymbol{u}_b - \boldsymbol{u}_c)}{\delta x} , \tag{SI.25}$$

which results in:

$$\boldsymbol{n} \cdot \boldsymbol{u}_b = \boldsymbol{n} \cdot \boldsymbol{u}_c . \tag{SI.26}$$

Equation (SI.23) is also discretized using a linear interpolation scheme:

$$\mathbf{T} \cdot \boldsymbol{u}_b = -\mathbf{T} \cdot \left(\ell \frac{\boldsymbol{u}_b - \boldsymbol{u}_c}{\delta x} \right) = \mathbf{T} \cdot \left(\ell \frac{\boldsymbol{u}_c}{\delta x + \ell} \right) . \tag{SI.27}$$

The final form of the BC is then implemented as a Dirichlet BC:

$$\boldsymbol{u}_b = \boldsymbol{n}(\boldsymbol{n} \cdot \boldsymbol{u}_b) + \mathbf{T} \cdot \boldsymbol{u}_b = \boldsymbol{n}(\boldsymbol{n} \cdot \boldsymbol{u}_b) + \mathbf{T} \cdot \left(\ell \frac{\boldsymbol{u}_c}{\delta x + \ell} \right) . \tag{SI.28}$$

This formulation clearly requires multiple fixed point iterations that, if they converge, result in the correct calculation of $\boldsymbol{u}_p$ up to second-order accuracy. For the pressure field, we employ a *fixedFluxPressure* BC, which essentially imposes a pressure gradient based on the flux leaving the domain, and allows the simulation to self-consistently determine the wall permeation velocity.

Since study steady flow, the initial conditions are only relevant for the convergence (rather than the accuracy), so they are simply specified as zero velocity and zero pressure. That is, we assume the fracture is fill with fluid at rest. At the inlet of the fracture ($x = 0$), we impose the theoretically computed velocity profile given by Eqs. (SI.7) and (SI.10) (with dp^*/dx^* computed from Eq. (SI.16) under the constraint $\langle u^* \rangle = 1$), which has a non-zero permeation velocity and satisfies the BJS BC at the inlet's walls ($z = \pm h_0$). A zero-gradient velocity BC is employed across the outlet plane ($x = L$), and the pressure there is set to zero gauge pressure (see Fig. S2). We do not consider the case of a closed fracture, so we do not need to impose a crack-tip condition.

To find the optimal computational grid arrangement for the simulations results presented in the main text, we ran a series of test cases with different numbers of grid elements and with different grid resolutions (spacing), as summarized in Table S1. The simulations can be considered non-dimensional (the fluid's physical properties are chosen to fix the dimensionless parameters such as $\tilde{Re}$). To maintain ϵ, the simulation channel has length $L = 100$ and inlet half-depth $h_0 = 1$. From each simulation, we extracted the velocities at the cross-sectional plane located at $x^* = 0.5$. We also extracted the pressure gradient dp^*/dx^* variation along the whole channel. Then, we calculated the percent

change of these quantities with respect to the theoretical values (see above). Finally, the velocities from the simulations were rescaled by $\langle u \rangle$ to be comparable to the theory, since the constraint $\langle u \rangle = 1$ was imposed in the derivation.

The grid independence study revealed that the optimal choice is 4000 grid elements with $\Delta x = 0.5$ and $\Delta z = 0.05$, as it showed significantly better performance on the permeation velocity than coarser girds and finer grids did not improve the accuracy notably (see Fig. S4). The slip velocity and axial pressure gradient showed convergence for 4000 grid elements, with the error increasing for larger grids. Therefore, we used 4000 grid elements for all DNS results reported in the main text. Note that a non-uniform grid spacing (see Fig. S5) was used in the vertical direction to better resolve the flow near the porous walls.

References

Beavers, G. S., & Joseph, D. D. (1967). Boundary conditions at a naturally permeable wall. *J. Fluid Mech.*, *30*, 197–207. doi: 10.1017/S0022112067001375

Layton, W. J., Schieweck, F., & Yotov, I. (2002). Coupling fluid flow with porous media flow. *SIAM J. Numer. Anal.*, *40*, 2195–2218. doi: 10.1137/S0036142901392766

Mohais, R., Xu, C., Dowd, P. A., & Hand, M. (2012). Permeability correction factor for fractures with permeable walls. *Geophys. Res. Lett.*, *39*, L03403. doi: 10.1029/2011GL050519

Moukalled, F., Mangani, L., & Darwish, M. (2016). *The Finite Volume Method in Computational Fluid Dynamics: An Advanced Introduction with OpenFOAM® and Matlab*. Cham, Switzerland: Springer International Publishing. doi: 10.1007/978-3-319-16874-6

Saffman, P. G. (1971). On the boundary condition at the surface of a porous medium. *Stud. Appl. Math.*, *50*, 93–101. doi: 10.1002/sapm197150293

The OpenFOAM Foundation Ltd. (2020). *OpenFOAM.* Retrieved from `http://www.openfoam.org`

Weller, H. G., Tabor, G., Fureby, C., & Jasak, H. (1998). A tensorial approach to computational continuum mechanics using object-oriented techniques. *Comput. Phys.*, *12*, 620–631. doi: 10.1063/1.168744

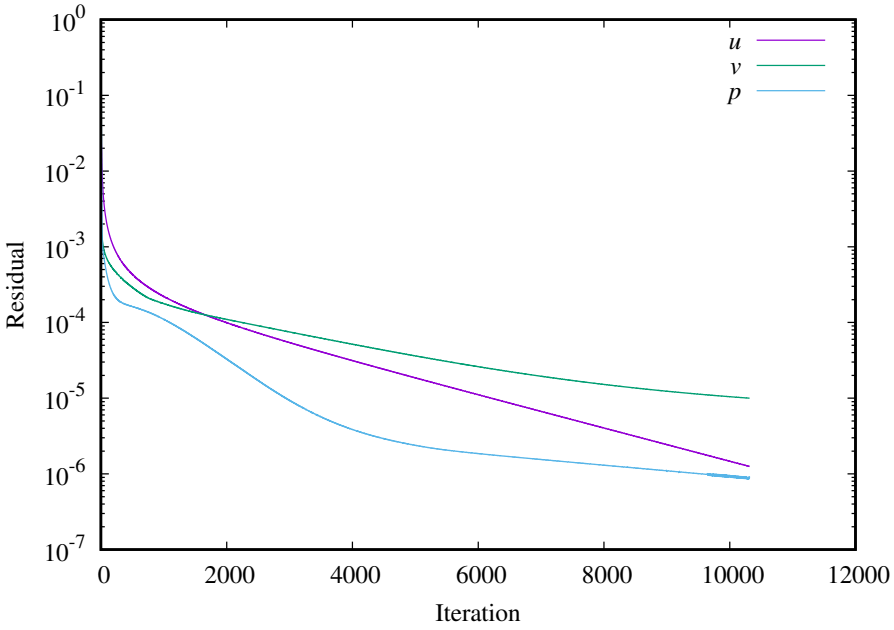

Figure S1. SIMPLE algorithm's residuals plot for a sample simulation with $\alpha = -10^{-3}$, $\phi = 5 \times 10^{-4}$ and $\tilde{Re} = 0.01$. The tolerance used is 10^{-5} for both the pressure residual and each velocity component's residual. The simulation converges after about 10000 iterations.

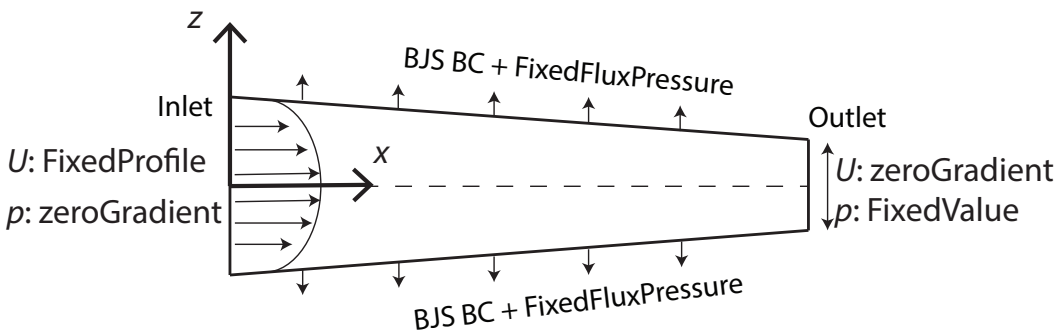

Figure S2. Schematic of the OpenFOAM® boundary conditions used in the numerical simulations.

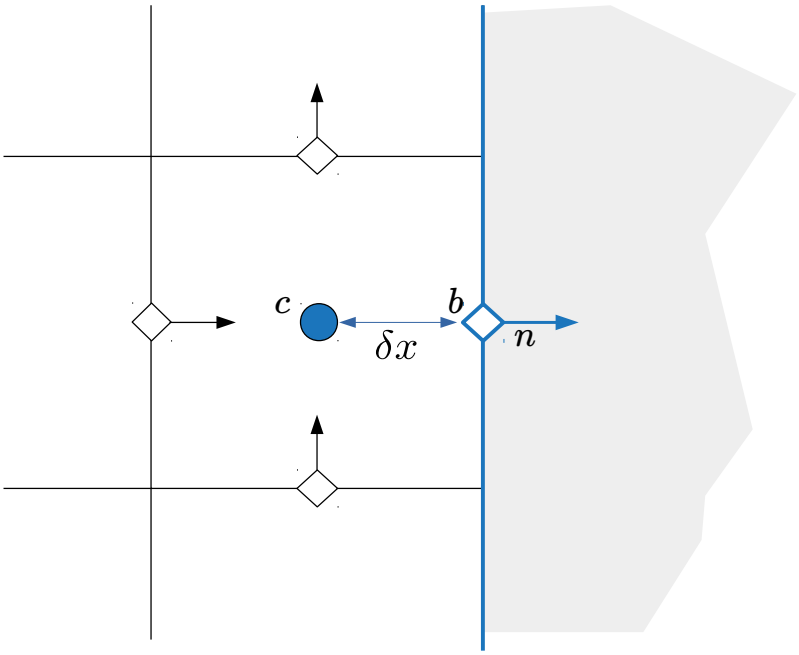

Figure S3. Illustration of a boundary cell with face centers an face normals. In this figure, c is the cell center (blue dot) and the blue line represents the boundary. The BJS BC is applied at point b, corresponding to the center of the boundary face, where δx is the distance between b and c, and n is the vector normal to the boundary face.

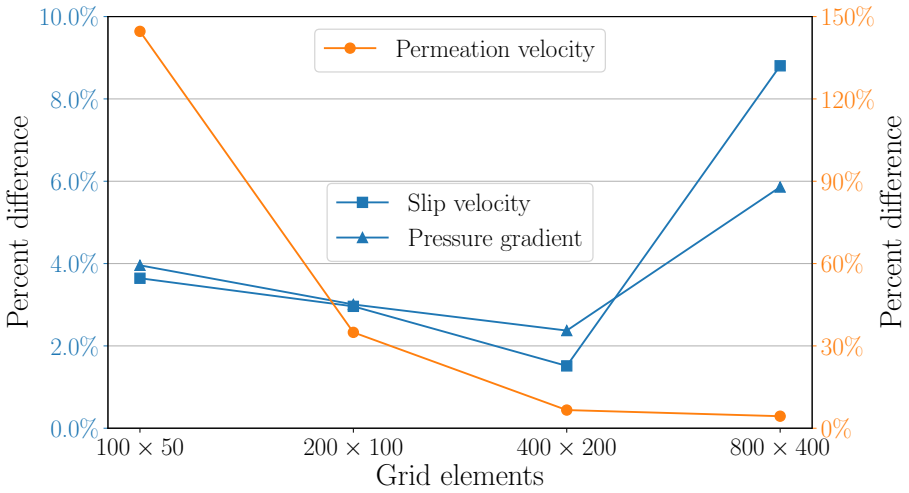

Figure S4. Grid independence of key flow quantities. Percent difference (relative to the theoretical solution in the main text) of the wall permeation velocity $v^*\big(x^*, h^*(x^*)\big)$, the wall slip velocity $u^*\big(x^*, h^*(x^*)\big)$, and the axial component of the pressure gradient dp^*/dx^*, all evaluated at $x^* = 0.5$ but using different grids.

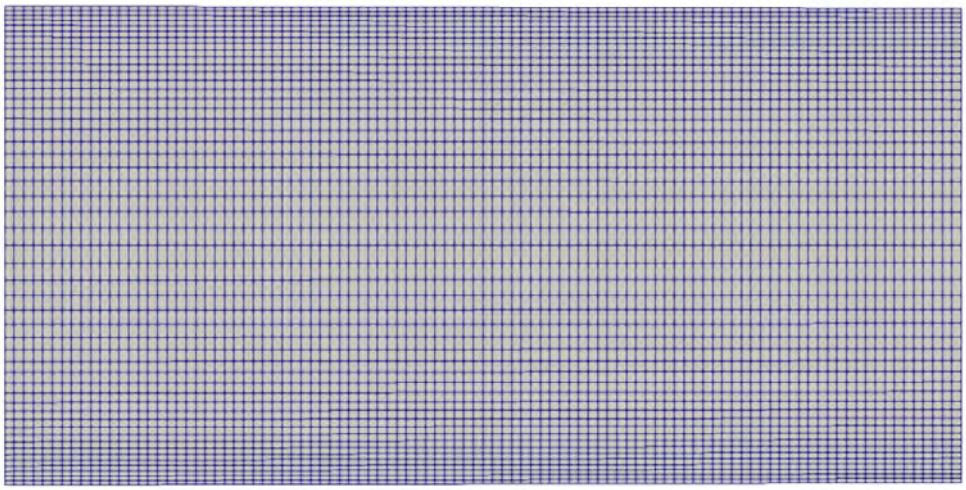

Figure S5. Numerical grid showing schematic the non uniform vertical spacing ("boundary layer meshing"). Notice that the grid spacing is scaled in the horizontal direction to fit the figure.

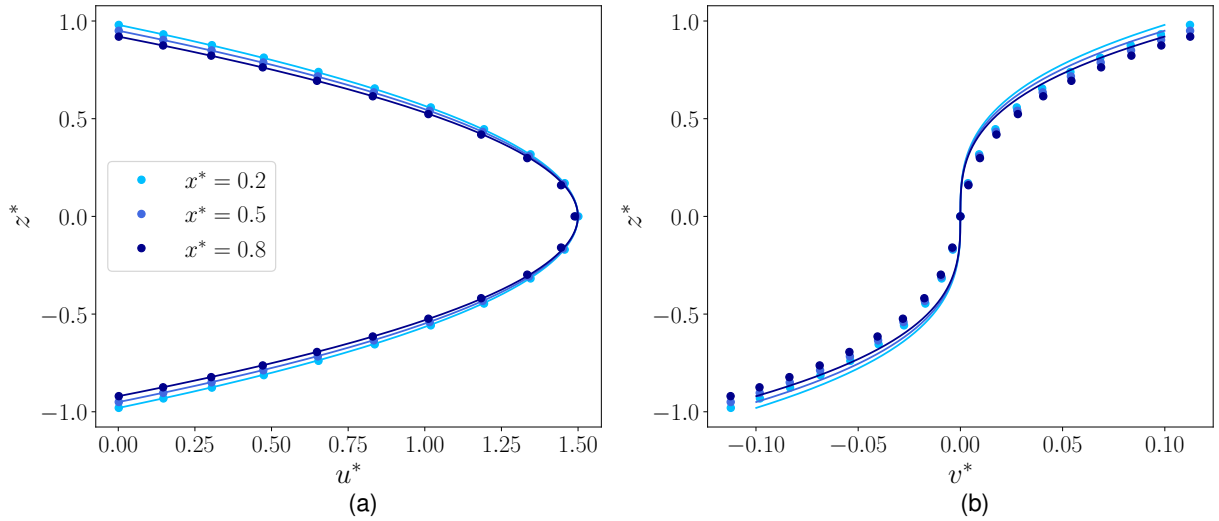

Figure S6. Flow-wise variation: Velocity profiles versus fracture depth z^* at the planes $x^* \in \{0.2, 0.5, 0.8\}$, for $\alpha = -10^{-3}$, $\phi = 10^{-4}$ and $\tilde{Re} = 0.01$: (a) the horizontal component $u^*(x^*, z^*)$; (b) the vertical component $v^*(x^*, z^*)$. Solid curves are the theoretical profiles from Eq. (SI.11), and filled circles with the same colors are the corresponding simulation results. Profiles are color-coded by their x^* positions.

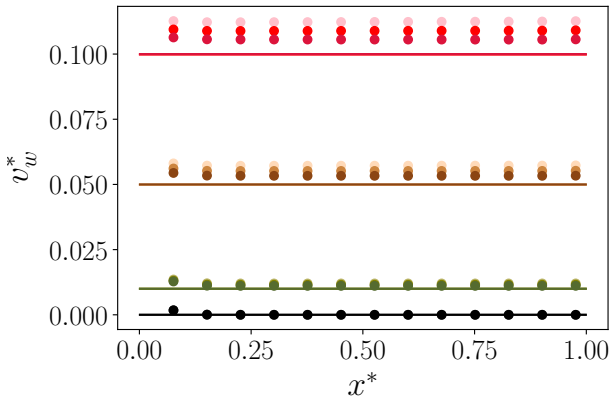

Figure S7. The wall permeation velocity $v_w^*(x^*)$ along the channel for $\tilde{Re} = 0.01$. Colors represent cases with different α and ϕ values: ●●●: $\alpha = 0$, $\phi \in \{0, 5 \times 10^{-4}, 10^{-3}\}$; ●●●: $\alpha = -10^{-4}$, $\phi \in \{0, 5 \times 10^{-4}, 10^{-3}\}$; ●●●: $\alpha = -5 \times 10^{-3}$, $\phi \in \{0, 5 \times 10^{-4}, 10^{-3}\}$; ●●●: $\alpha = -10^{-3}$, $\phi \in \{0, 5 \times 10^{-4}, 10^{-3}\}$. Filled circles represent the simulation results, and solid curves of the same color represent the corresponding theoretical predictions.

Table S1. Information about the grids used to establish grid independence of the direct numerical simulation results.

Grid arrangement	100×50	200×100	400×200	800×400
Total grid elements	5 000	20 000	80 000	320 000
Δx resolution	1	0.5	0.25	0.125
Δz resolution	0.02	0.01	0.005	0.0025